Numerical studies of femtosecond carrier dynamics in GaAs

D. W. Bailey and C. J. Stanton
Department of Physics, University of Florida, Gainesville, Florida 32611

K. Hess
Beckman Institute, University of Illinois, Urbana, Illinois 61801

(Received 30 March 1990)

We present simulations of 2-eV femtosecond differential transmission experiments in GaAs. Electron and heavy-, light-, and split-off-hole dynamics are calculated by an ensemble Monte Carlo method. To account for valence-band nonparabolicity and anisotropy, a 30-band $\mathbf{k}\cdot\mathbf{p}$ method is used to determine hole band structure, optical matrix elements, density of states, and Bloch overlap factors. Using the distribution functions obtained from the Monte Carlo simulations, we calculate the differential transmission and compare directly with experimental spectra. We show that the inclusion of both collisional broadening during photoexcitation and holes is essential to reproduce accurately the experimental results. We also discuss the effects of intervalley and carrier-carrier scattering in these measurements.

I. INTRODUCTION

Laser spectroscopy is arguably the best method for measuring carrier distribution functions in bulk GaAs. Unlike a dc transport measurement, which integrates over the entire distribution function, laser spectroscopy can selectively probe the energy dependence of the carrier density. *Time-dependent* laser spectroscopy has the additional advantage of studying the evolution of the distributions, and thus the carrier relaxation processes. Because of recent advances in femtosecond laser spectroscopy, particularly in tunable and continuum probe techniques,[1-6] distribution functions can be probed on the same time scale on which carrier scattering occurs. By studying these systems, detailed information about band structure, nonequilibrium relaxation processes, and scattering rates can be obtained.

Quantitative analysis of the data from 2-eV femtosecond laser spectroscopy, however, is difficult. Nonequilibrium carrier dynamics in GaAs is intricate because of many scattering mechanisms, multiple conduction-band minima, and three hole bands. Analysis of the nonlinear absorption is also demanding because it depends on the band structure as well as the distribution functions. These complications have led to apparently conflicting conclusions between experiments.[7-9]

Correctly and quantitatively interpreting femotosecond spectroscopy in GaAs, however, is possible if the carrier dynamics and nonlinear absorption are calculated accurately. To do this, our method is to model electron and hole relaxation simultaneously by an ensemble Monte Carlo simulation. The time-dependent distribution functions from the Monte Carlo simulation are then used to evaluate the differential transmission. By directly matching experimental results over a large range of energies we demonstrate the validity of our model and at the same time obtain the most accurate interpretation of these experiments to date.

From our calculations we arrive at several important conclusions.

(i) The differential transmission cannot be assessed without including holes in both the carrier dynamics and nonlinear absorption calculations.

(ii) To get the correct correspondence to experiment, collisional broadening must be included in the determination of nonlinear absorption, otherwise the calculated initial transient transmission at the pump energy is too large.

(iii) Our band-structure calculations show that the effective-mass approximation for holes is invalid in these simulations. Anisotropy and nonparabolicity are too large over the range of energies which are considered to assign a meaningful set of hole effective masses.

(iv) The width of the transient transmission peak for 2-eV photoexcitation in GaAs is highly sensitive to intervalley scattering, and insensitive to electron-electron scattering. The best fit with experimental results occurs for the intervalley deformation potential constant given by $D_{\Gamma\to L}=5\times10^8$ eV/cm.

In the next section we describe our approach to calculating the differential transmission. Since Monte Carlo methods have been discussed thoroughly in the literature, emphasis is placed on the calculations involving band structure and nonlinear absorption. Results of the simulated differential transmission spectra for pump–continuum-probe and 2-eV pump-probe experiments are presented in Sec. III. Conclusions are given in Sec. IV.

II. CALCULATIONAL METHOD

There are two common procedures for analyzing results from 2-eV femtosecond laser spectroscopy in GaAs: the extracted time-constant method, and solving the Boltzmann transport equation to simulate the relaxation of photoexcited carriers.

In the extracted time-constant method the experimental differential transmission is fitted to the convolution of a set of one-sided exponential time decays, with different maximum heights, and the probe-pulse autocorrelation. One to three decays, or time constants, are extracted from the experimental data and directly attributed to a set of plausible scattering mechanisms. This method is based on the assumption that a standard multilevel system response model[10,11] can be applied to GaAs to describe carrier relaxation. The extracted time-constant method, however, oversimplifes the carrier dynamics and provides misleading results when applied to 2-eV photoexcitation in GaAs because of competing scattering processes and nonisolated levels. Scattering mechanisms that occur on the same time scale are indistinguishable in the measurement, and carriers that relax out of initially excited levels sometimes reenter those same or equivalent levels. For these reasons and because scattering rates depend on energy, the extracted time-constant method is inadequate and misleading for explaining the data from femtosecond laser spectroscopy experiments.[12]

The second conventional procedure for interpreting high-energy femtosecond laser spectroscopy is to solve the Boltzmann transport equation, either directly[13–16] or using the Monte Carlo method.[17–19] Comparisons to experiments, if included at all, are in the form of estimating time constants from the evolution of the distribution function. Typically, only the photoexcited electrons are modeled. This method used by itself has limited success because of the weak connection to experimental results. Although carrier dynamics are modeled in a sophisticated manner, nonlinear absorption effects are not treated numerically and conclusions are necessarily qualitative. That is, the joint density of states, optical matrix elements, time convolution, and energy integral of the probe pulse, and summation over optical transitions are neglected in these treatments when a link to experiment is suggested.

Our approach is to use an ensemble Monte Carlo method to model both electron and hole dynamics, and, in addition, to couple these simulations to calculations of the nonlinear absorption. To account for the difficulties of modeling holes, we use a $\mathbf{k}\cdot\mathbf{p}$ method[20,21] to calculate the hole band structure, optical matrix elements, density of states, and Bloch overlap factors. Our goal is to quantitatively interpret femtosecond laser spectroscopy experiments. Thus the extracted time constant method is avoided, and instead nonlinear absorption calculations are compared directly with the experimental results.

To summarize our method of simulation, the band structure and related variables, such as Bloch overlap factors, are determined from the $\mathbf{k}\cdot\mathbf{p}$ method. The nonlinear absorption is then calculated to determine initial photoexcited electron-hole pair states generated by the pump pulse. Carrier dynamics is then determined by an ensemble Monte Carlo simulation. The final step is calculating the differential transmission using the distribution functions from the completed Monte Carlo simulation.

A. Band structure

The band structure governs the calculation of both the absorption profile and carrier-scattering rates. The optically connected region is determined by energetically allowed optical transitions, and $E(\mathbf{k})$ is needed in the calculation of scattering rates and the final state after each scattering event.

For electrons the effective-mass approximation is appropriate and expeditious, so we use a three-valley analytic model for the conduction band. The Γ valley is treated isotropically and includes nonparabolicity, i.e., $E(1+\alpha E)=\hbar^2k^2/2m^*$, where α is a nonparabolicity constant (cf. Table I). The L and X valleys are treated as ellipses.

For the range of energies under consideration, however, for the holes the effective-mass approximation is invalid. Anisotropy and nonparabolicity are too large. Therefore, for the heavy-, light-, and split-off-hole bands we diagonalize a full-zone 30×30 $\mathbf{k}\cdot\mathbf{p}$ Hamiltonian following the procedure of Pollak *et al.*[21] $\mathbf{k}\cdot\mathbf{p}$ parameters for 300-K GaAs are chosen to match the conduction-band effective mass ($m_c^*=0.064m_0$), and the direct energy gaps between split-off and heavy-hole bands ($\Delta_0=0.34$ eV) and between heavy-hole and conduction bands ($E_0=1.424$ eV).[22–24] Band-structure parameters used in the Monte Carlo and nonlinear absorption calculations are shown in Table I. The input parameters to the $\mathbf{k}\cdot\mathbf{p}$ program are shown in Table II.

The band structure between the main symmetry points

TABLE I. Band-structure values obtained from $\mathbf{k}\cdot\mathbf{p}$ calculations compared with values reported in the literature (which are labeled as "explicit"). In these simulations we use explicit values for the conduction band. Effective masses in the L and X directions, denoted by $\langle 111\rangle$ and $\langle 100\rangle$, respectively, are included to show the degree of anisotropy of the hole bands.

Parameter	$\mathbf{k}\cdot\mathbf{p}$	Explicit
E_0 (eV)	1.421	1.424 (Ref. 24)
Δ_0 (eV)	0.339	0.340 (Ref. 23)
$E_{\Gamma L}$ (eV)	0.31	0.31 (Ref. 22)
$E_{\Gamma X}$ (eV)	0.45	0.49 (Ref. 22)
m_c^*	0.067	0.063 (Ref. 22)
$\alpha^{(a)}$ (eV^{-1})		0.64 (Ref. 22)
m_{tL}^*		0.12 (Ref. 46)
m_{lL}^*		1.47 (Ref. 46)
m_{tX}^*		0.237 (Ref. 46)
m_{lX}^*		1.58 (Ref. 46)
$\langle 111\rangle^{(b)}$ m_{hh}^*	1.07	
$\langle 100\rangle^{(c)}$ m_{hh}^*	0.37	
$m_{hh}^{*(d)}$	0.68	
$\langle 111\rangle^{(b)}$ m_{lh}^*	0.076	
$\langle 100\rangle^{(c)}$ m_{lh}^*	0.088	
$\langle 111\rangle^{(b)}$ m_{so}^*	0.172	
$\langle 100\rangle^{(c)}$ m_{so}^*	0.171	

[a] α is a Γ-valley nonparabolicity factor used in the dispersion relation $E(1+\alpha E)=\hbar^2k^2/2m^*$.

[b] $\lim_{k\to0}|\hbar^2/\partial^2E/\partial k^2|$, defined for k along Γ to L.

[c] $\lim_{k\to0}|\hbar^2/\partial^2E/\partial k^2|$, defined for k along Γ to X.

[d] The scalar effective mass for an anisotropic valley is not clearly defined. The value shown is given by $(m^*_{\langle 111\rangle})^{3/7}(m^*_{\langle 100\rangle})^{4/7}$ to represent weighting in the L and X directions.

TABLE II. $\mathbf{k}\cdot\mathbf{p}$ input parameters used to get the $\mathbf{k}\cdot\mathbf{p}$ values shown in Table I. Nomenclature can be found in Pollak *et al.* (Ref. 21). With the exceptions of $\Gamma_{2'}^{l}$, P, Δ_{25}', and the matrix elements of V^{-}, the values remain close to those chosen by Pollak *et al.* (Ref. 21). These particular values are changed to match reported values of the conduction-band effective mass (m^*), the direct energy gap between split-off- and heavy-hole bands (Δ_0), and the direct energy gap between heavy-hole and conduction bands (E_0).

Parameter	GaAs
$\Gamma_{2'}^{l}$	0.0658
Γ_{15}	0.232
Γ_{1}^{u}	0.571
$\Gamma_{12'}$	0.771
$\Gamma_{25'}^{u}$	1.25
$\Gamma_{2'}^{u}$	1.35
Γ_{1}^{l}	−0.966
$2i\langle\Gamma_{25'}^{l}\vert\mathbf{p}\vert\Gamma_{2'}^{l}\rangle\equiv P$	1.25
$2i\langle\Gamma_{25'}^{l}\vert\mathbf{p}\vert\Gamma_{15}\rangle\equiv Q$	1.07
$2i\langle\Gamma_{25'}^{l}\vert\mathbf{p}\vert\Gamma_{12'}\rangle\equiv R$	0.8049
$2i\langle\Gamma_{25'}^{l}\vert\mathbf{p}\vert\Gamma_{2'}^{u}\rangle\equiv P''$	0.1
$2i\langle\Gamma_{25'}^{u}\vert\mathbf{p}\vert\Gamma_{2'}^{l}\rangle\equiv P'$	0.1715
$2i\langle\Gamma_{25'}^{u}\vert\mathbf{p}\vert\Gamma_{15}\rangle\equiv Q'$	−0.752
$2i\langle\Gamma_{25'}^{u}\vert\mathbf{p}\vert\Gamma_{12'}\rangle\equiv R'$	1.4357
$2i\langle\Gamma_{25'}^{u}\vert\mathbf{p}\vert\Gamma_{2'}^{u}\rangle\equiv P'''$	1.6231
$2i\langle\Gamma_{1}^{u}\vert\mathbf{p}\vert\Gamma_{15}\rangle\equiv T$	1.2003
$2i\langle\Gamma_{1}^{l}\vert\mathbf{p}\vert\Gamma_{15}\rangle\equiv T'$	0.5323
Δ_{25}'	0.0293
Δ_{15}	0.0265
$V_1^{-}(\langle\Gamma_{15}\vert V^{-}\vert\Gamma_{25'}^{l}\rangle)$	0.1270
$V_2^{-}(\langle\Gamma_{2'}^{l}\vert V^{-}\vert\Gamma_{1}^{u}\rangle)$	−0.2174
$V_3^{-}(\langle\Gamma_{2'}^{l}\vert V^{-}\vert\Gamma_{1}^{l}\rangle)$	0.3344
$V_4^{-}(\langle\Gamma_{15}\vert V^{-}\vert\Gamma_{25'}^{u}\rangle)$	0.1525
$V_5^{-}(\langle\Gamma_{2'}^{u}\vert V^{-}\vert\Gamma_{1}^{u}\rangle)$	−0.4087
$V_6^{-}(\langle\Gamma_{2'}^{u}\vert V^{-}\vert\Gamma_{1}^{l}\rangle)$	0.0
Δ^{-}	0.0050

obtained with the $\mathbf{k}\cdot\mathbf{p}$ method are shown in Fig. 1. Because it is a perturbative method, the band structure from the $\mathbf{k}\cdot\mathbf{p}$ calculation is most reliable at the zone center,[25] the only portion of the band structure needed in the simulations. Another advantage is that the $\mathbf{k}\cdot\mathbf{p}$ method is faster than most band-structure calculation methods.

For 2-eV photoexcitation in GaAs, only the conduction band and heavy-, light-, and split-off-hole bands are involved. The band structures for these four bands along the Λ- and Δ-symmetry lines are enlarged in Figs. 2(a) and 2(b), respectively. Vertical arrows show the three-electron optical transitions allowed for 2-eV photoexcitation. The light-hole transition to the conduction band occurs beyond the first inflection point away from the center of the zone, showing it is wrong to use a simple effective mass for the light holes. $\Gamma\rightarrow L$ and $\Gamma\rightarrow X$ intervalley scattering, two of the primary ways electrons are removed from the optically connected region, are represented by the horizontal arrows. The electrons excited from the split-off band do not have enough energy to undergo intervalley scattering.

Figure 3 shows the heavy-hole band structure close to the Γ valley in the $k_z=0$ plane. Significant anisotropy is

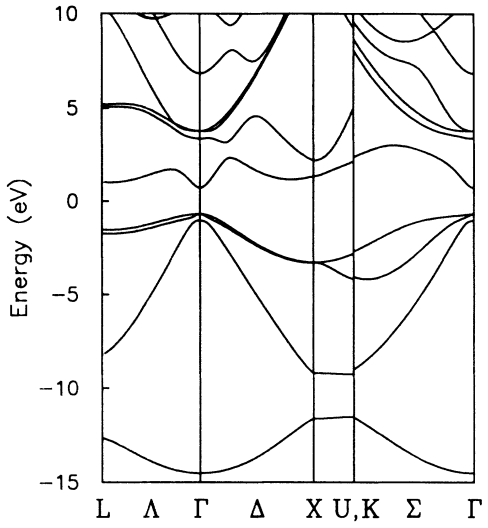

FIG. 1. Energy bands for GaAs obtained from the 30-band $\mathbf{k}\cdot\mathbf{p}$ method. The matrix elements for the Hamiltonian are determined so that the band gap, spin-orbit splitting, and carrier effective masses agree with experimental values.

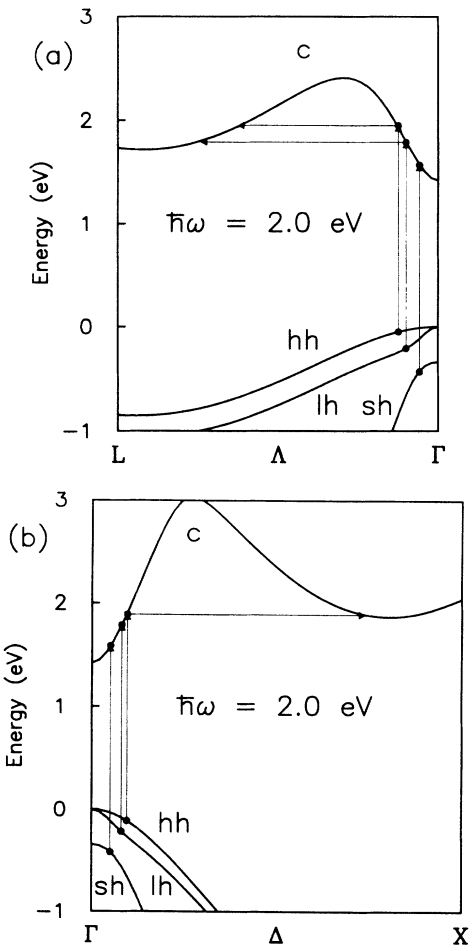

FIG. 2. The (top to bottom) conduction, heavy-hole, light-hole, and split-off-hole bands for GaAs in the (a) L- and (b) X-point directions. 2-eV optical transitions and intervalley scattering are represented by vertical and horizontal arrows, respectively.

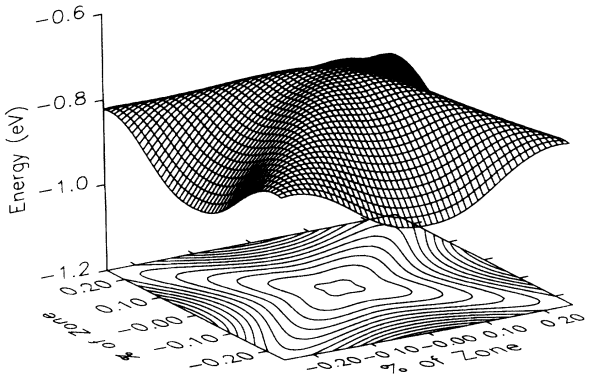

FIG. 3. Heavy-hole energy surface and equal-energy contours in the $k_z=0$ plane calculated from the $\mathbf{k}\cdot\mathbf{p}$ method. For 2-eV photoexcitation in GaAs carriers are generated in the heavy-hole band more than 10% away from the zone center.

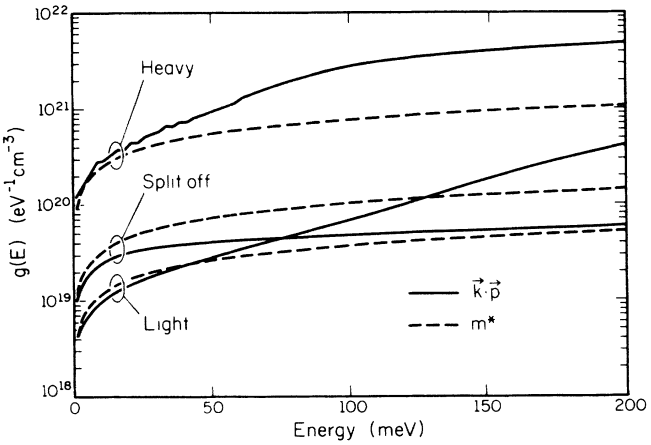

FIG. 4. Density of states for heavy-, split-off-, and light-hole bands comparing the $\mathbf{k}\cdot\mathbf{p}$ method with the effective-mass approximation. For holes the effective-mass approximation is valid only near the band edge.

displayed even at low energies, again showing the inappropriateness of the effective-mass approximation for the holes.

$E_v(\mathbf{k})$ is calculated by the $\mathbf{k}\cdot\mathbf{p}$ program at mesh points in a $\frac{1}{48}$ irreducible wedge of the Brillouin zone. During the simulation, $E_v(\mathbf{k})$ is propagated by cubic symmetry into the first octant of the Brillouin zone and found by interpolation using nearest neighbors in the axis directions. The eigenstates are used to determine allowable optical transitions, density of states, joint density of states between conduction and hole bands, and final states for each scattering event. The eigenfunctions are used to calculate optical matrix elements and Bloch overlap factors.

1. *Density of states*

From Fermi's golden rule, the transition rate is proportional to the density of final states. We use the density of states, $g_v(E)$, in the calculation of hole deformation potential phonon scattering rate. The joint density of states, $\rho_v(E)$, is used to calculate the nonlinear absorption.

In the effective-mass approximation, the density of states is $g(E)dE=(1/\pi^2)(m^*/\hbar^2)^{3/2}\sqrt{2E}\,dE$. The joint density of states is given by the same expression, except that m^* is replaced by $\mu=(1/m_c^*+1/m_v^*)^{-1}$, where c and v subscripts denote conduction and valence bands, respectively. Since for holes at large energies the effective-mass approximation is invalid, we calculate the density of states and the joint density of states by

$$g_v(E)dE=\frac{1}{4\pi^3}\int_{S(E)}\frac{dS}{|\nabla_{\mathbf{k}}E_v(\mathbf{k})|} \tag{1}$$

and

$$\rho_v(E)dE=\frac{1}{4\pi^3}\int_{S(E)}\frac{dS}{|\nabla_{\mathbf{k}}[E_c(\mathbf{k})+E_v(\mathbf{k})]|}\ , \tag{2}$$

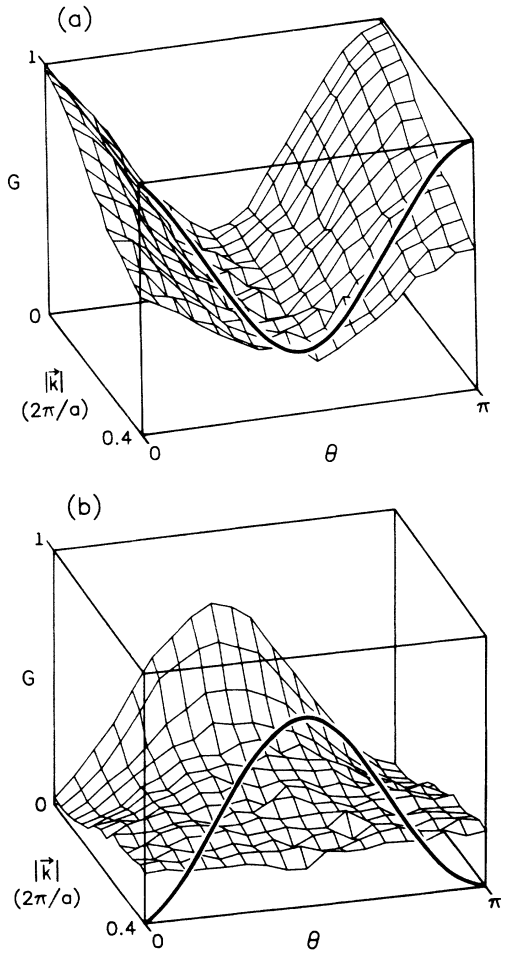

FIG. 5. (a) Heavy-hole–heavy-hole Bloch overlap factors calculated from the $\mathbf{k}\cdot\mathbf{p}$ method compared with the intraband Wiley approximation (Ref. 31) (shown on the front face). Factors are plotted for small k as a function of the angle between $\mathbf{k}$ and $\mathbf{k}'$ for k' from 0 to 40% of Γ–X. (b) Light-hole–heavy-hole Bloch overlap factors calculated from the $\mathbf{k}\cdot\mathbf{p}$ method compared with the interband Wiley approximation (Ref. 31).

where $S(E)$ is an isoenergy surface in $\mathbf{k}$ space. The Brillouin zone is divided into a cubic mesh, and $E(\mathbf{k})$ and $dE/d\mathbf{k}$ are calculated by the $\mathbf{k}\cdot\mathbf{p}$ method for the center of each cell. Assuming $E(\mathbf{k})$ changes uniformly and in a planar manner over each cell, the area of the isoenergy plane intersecting each cell is determined according to the method of Gilat *et al.*,[26,27] and the integrations over all $S(E)$ in Eqs. (1) and (2) are performed. The approximation improves with the number of cells that $S(E)$ includes. Figure 4 compares $g_v(E)$ calculated using the $\mathbf{k}\cdot\mathbf{p}$ method versus the effective-mass approximation. Because of nonparabolicity and anisotropy, for holes the effective-mass approximation is appropriate only near the band edge.

2. *Bloch overlap factors*

Bloch overlap factors, the inner product of the periodic part of the initial and final Bloch states, must be included in the calculation of hole-scattering rates. Although the Bloch overlap factors can be approximated as unity for electron interactions, they vary between 0 and 1 for holes. The usual approximation, taken by several researchers[19,28,29] and valid for $k \rightarrow 0$,[30] is to use Wiley's approximation for interactions involving light and heavy holes based on a four-band $\mathbf{k}\cdot\mathbf{p}$ method,[31]

$$G_{\text{lh-lh}} = G_{\text{hh-hh}} = \tfrac{1}{4}(1+3\cos^2\theta) , \tag{3a}$$

$$G_{\text{lh-hh}} = G_{\text{hh-lh}} = \tfrac{3}{4}\sin^2\theta , \tag{3b}$$

where θ is the angle between $\mathbf{k}$ and $\mathbf{k}'$. Wiley's expressions,[31] however, are not intended for interactions involving the split-off band and are a poor approximation for high-energy holes in any of the bands.

Bloch overlap factors for small k' heavy-hole–heavy-hole (hh-hh) interactions and light-hole–heavy-hole (lh-hh) interactions as a function of k and θ are shown in Fig. 5. Significant differences between the calculated results and Wiley's approximation,[31] shown on the front face for comparison, occur away from the band edge. The Appendix provides details of how G is calculated from the $\mathbf{k}\cdot\mathbf{p}$ method.

The rejection method is used to implement the Bloch overlap factors in the Monte Carlo simulation,[29] similar to the usual application of the Pauli exclusion principle.[32] Thus the overlap factor is included by a Monte Carlo integration of the matrix element. If a hole is selected to scatter, its final state and Bloch overlap factor are calculated. If the overlap factor is less than a random number uniformly distributed between 0 and 1, then the scattering event is rejected.

B. Nonlinear absorption

A critical part of our model is the calculation of the nonlinear absorption. It is used not only to determine the differential transmission, it is also needed to determine the initial states for the excited electron-hole pair. The expression for the differential absorption is obtained by summing the number of photons over allowed optical transitions assuming Fermi's golden rule,

$$\alpha(t) \propto \frac{1}{\omega}\int d\hbar\omega \int dt' N(\hbar\omega, t-t') \sum_v \int d\mathbf{k} |H_{\mathbf{k}}|^2 \delta(E_c(\mathbf{k}) - E_v(\mathbf{k}) - \hbar\omega)[1 - f_c^e(\mathbf{k},t') - f_v^h(\mathbf{k},t')] . \tag{4}$$

Therefore,

$$\Delta\alpha(t) \propto -\frac{1}{\omega}\int d\hbar\omega \int dt' N(\hbar\omega, t-t') \sum_v |H_v(\hbar\omega)|^2 \rho_v(\hbar\omega)[f_c^e(\hbar\omega,t') + f_v^h(\hbar\omega,t')] , \tag{5}$$

where $N(\hbar\omega,t)$ is the transient photon-energy density. By $f(\hbar\omega,t)$ we mean the time-dependent distribution function in the optically connected region, which should not be confused with $f(E,t)$. If conduction and valence bands are isotropic, then

$$f(E,t)dE = f(\hbar\omega,t)d\hbar\omega ,$$

i.e., then the distributions in the optically connected region are proportional to the energy distributions. To simplify the calculation we approximate the optical matrix element $|H_{\mathbf{k}}|^2$ in Eq. (4) by $|H_v(\hbar\omega)|^2$ in Eq. (5). To calculate the optical matrix elements we average over polarizations. As expected, $|H_v(\hbar\omega)|^2$ decreases with increasing energy as the coupling between the bands decreases. To evaluate $\Delta\alpha(t)$, the rejection method is used for each term in the integrand of Eq. (5).

In the thin-sample limit, the expression for the differential transmission is derived from Eq. (5) as

$$\frac{\Delta T(t)}{T_0} \propto \frac{1}{\omega}\int d\hbar\omega \int dt' N(\hbar\omega, t-t') \sum_v |H_v(\hbar\omega)|^2 [n_c^e(\hbar\omega,t') + n_v^h(\hbar\omega,t')] , \tag{6}$$

where $n(\hbar\omega,t)$ is the time-dependent density of carriers in the optically connected region as given by the Monte Carlo simulations. Equation (6) is calculated more efficiently than Eq. (5) since the rejection technique is used only to generate $N(\hbar\omega, t-t')$. Implicit in evaluation of Eq. (6), because it is calculated after the Monte Carlo simulation of the pump pulse, is the assumption that the probe pulse does not appreciably disturb the carrier populations. This is a reasonable approximation since for these experiments the intensity of the pump

pulse is several orders of magnitude larger than the intensity of the probe pulse.

Starting from no carriers 200 fs before the center of the pump pulse, electron-hole pairs are introduced in the simulation according to the transient photon energy density

$$N(\hbar\omega,t)=N_0 e^{-4\ln(2)(\hbar\omega-\hbar\omega_0)^2/\sigma^2} \times \mathrm{sech}^2\left[\frac{2t\cosh^{-1}(2)}{\tau_0}\right], \quad (7)$$

where $\hbar\omega_0$ is the spectral center of the laser pulse, and σ and τ_0 are the spectral and temporal full widths half maximums of the pulse intensity, respectively. For the simulations of equal-energy pump-probe experiments,[2] $\hbar\omega_0=1.98$ eV, $\sigma=40$ meV, and $\tau_0=40$ fs. For the simulations of continuum-probe experiments,[1] the pump pulse is set to $\hbar\omega_0=2.0$ eV, $\sigma=20$ meV, and $\tau_0=75$ fs. The continuum-probe pulse and tunable monochromator are modeled by 12 individual pulses with different central energies, $\sigma=15$ meV and $\tau_0=100$ fs. The pulse full widths at half maximum in the continuum-probe experiment[2] are not accurately known.

1. Collisional broadening

In addition to broadening due to the laser linewidth, there is also energy uncertainty in the initially excited states due to collisional broadening.[33,34] The expression for the nonlinear absorption [Eq. (4)] is therefore only valid in the long-time collisionless limit. To include the effects of collisions the δ function must be broadened. We approximate this by randomly distributing each carrier about its unbroadened initial state according to a Lorentzian. The spread of the Lorentzian is given by $\Delta E=\hbar/\tau(E)$, where $\tau(E)$ is the energy-dependent total scattering rate determined self-consistently from the Monte Carlo simulation. This type of broadening is about 10 meV, but varies significantly with energy and band. Figure 6 shows the broadening in each band as a function of energy at the temporal center of the pulse. An increase occurs for each line at $\sim$30 meV because of the onset of phonon emission.

Because of its lower density of states, the conduction band receives most of the broadening due to the laser linewidth. Unlike linewidth broadening, lifetime broadening is not shared between electron and hole bands, but instead is treated independently in each band. Thus, neglecting collisional broadening effects in a simulation makes the initial transient too large, especially for the heavy-hole contributions.

C. Monte Carlo method

The ensemble Monte Carlo method is described in detail in the literature.[32,35] In particular, we use a constant time step and include electron–polar-optical-phonon, electron–intervalley-phonon, Γ-valley-electron–electron, electron-hole, hole–polar-optical-phonon,[28,36] hole–nonpolar-optical-phonon,[28,37] and hole-hole scattering mechanisms. All types of hole scattering refer to heavy-, light-, and split-off-hole bands, and including both interband and intraband scattering. Other scattering mechanisms which occur on a picosecond scale or slower, such as acoustic scattering, are not included.

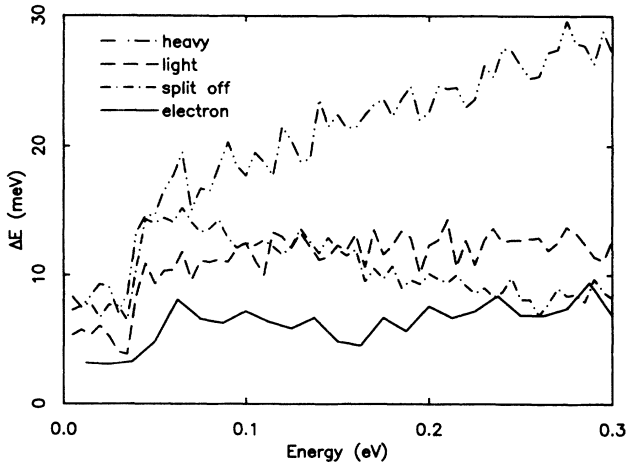

FIG. 6. Collisional broadening in each band as a function of carrier energy at $t=0$. Collisional broadening is given by $\Delta E=\hbar/\tau(E)$, where $\tau(E)$ is the total energy-dependent scattering rate determined from the Monte Carlo simulation. Carrier-phonon emission causes ΔE to increase at 30 meV.

III. RESULTS

Both pump-continuum probe[1] and 2-eV pump-probe experiments[2] are simulated. The validity of our model is established by comparisons of our results with the pump-continuum–probe spectra.[1] In addition, we show the importance of holes and collisional broadening by showing pump-continuum–probe spectra from simulations without those elements.

Because the transmission resolution of the 2-eV pump-probe experiments[2] is good, a quantitative comparison with calculated results is possible. Specifically, the importance of various scattering mechanisms is determined by observing the sensitivity of the differential transmission to changes in the scattering rates. This method shows that carrier-carrier scattering is unimportant in these measurements and that intervalley scattering has a large influence on the differential transmission.

A. Pump–continuum-probe simulations

The energy densities from the Monte Carlo simulations are shown first because they provide a basis for understanding the carrier dynamics. Equally important are plots showing the parts of the distribution functions which are probed at different energies, since the integral of the optically connected region and the distribution functions is a first-order estimate of the differential transmission [(cf. Eq. (6)]. We compare the experimental data with our calculated results, and then show results from simulations which elucidate the effects of collisional broadening and holes.

Figure 7(a) shows the electron-energy density for only the Γ valley for 75-fs, 2-eV photoexcitation. Three initial

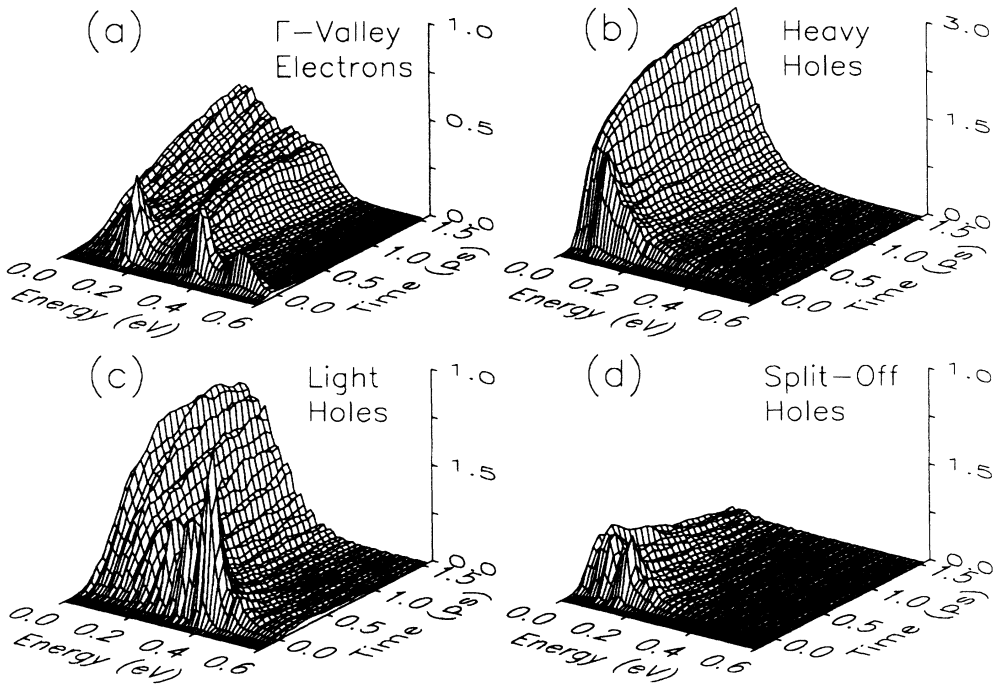

FIG. 7. Carrier density as a function of energy and time for (a) Γ-valley electrons, (b) heavy holes, (c) light holes, and (d) split-off holes for photoexcitation by a 75-fs pulse centered at $t=0$. (a) Three initial optical transitions are shown from (left to right) split-off-, light-, and heavy-hole bands. Because the heavy-hole band is more anisotropic than the other hole bands, the heavy-hole transition is broadest in energy. Intervalley scattering occurs quickly for electrons excited from the light- and heavy-hole bands, so the heights of the upper two peaks are suppressed. (b) A hot Maxwellian distribution forms quickly because of high scattering rates and because the transition occurs near the top of the band. (c) Because the transition occurs away from the top of the band, peaks due to phonon emission are shown. The number of light holes eventually decreases because of scattering to the heavy-hole band. (d) Intersubband scattering, mostly to the heavy-hole band, causes the total density of holes in the split-off band to decrease.

transitions from (left to right) split-off-, light-, and heavy-hole bands are shown near $t=0$. Intervalley scattering occurs quickly for electrons excited from the light- and heavy-hole bands, so the heights of the two higher-energy peaks are suppressed. The knee at 0.3 eV is from electrons returning to the Γ valley from the bottom of the L valleys.

Figure 7(b) shows the heavy-hole energy density rises quickly at the top of the band (at the lowest energy). A hot Maxwellian distribution forms quickly for the heavy holes because of high scattering rates and because the initial excitation is near the top of the band. The light- and split-off-hole density plots in Figs. 7(c) and 7(d) show some phonon structure because the photoexcitation peaks occur away from the band edges. The number of holes in these two bands decreases as they scatter to the heavy-hole band.

Figures 8(a) and 8(b) show the optically connected regions, or energy regions sampled, by the continuum probe, in conduction and heavy-hole bands, respectively. At energies above 1.73 eV, the split-off transition is not allowed. Both parts of Fig. 8 reveal the degree of anisotropy of the heavy-hole band. Although the optically connected region in the heavy-hole band is narrow, it changes energy depending on the direction in **k** space.

Results for the calculation of differential transmission as a function of probe delay and energy are shown in Fig. 9 along with the experimental results. Experimental data are shown in Fig. 9(a). Figure 9(b) shows the results of our Monte Carlo calculations including electrons and heavy-, light-, and split-off holes. Parameters in the Monte Carlo simulation have *not* been optimized. Agreement between theory and experiment is excellent.

Figures 9(c) and 9(d) show the contributions to the differential transmission of only the holes and of only the electrons, respectively. The hole differential transmission is the sum of the contributions from heavy-, light-, and split-off-hole bands. The hole differential transmission converges more quickly than the electron differential transmission, which shows a slowly increasing rate of rise in the contribution at low energy. The differential transmission for the electrons is lower at 1.73 eV than at 1.78 eV because the split-off transition is not allowed at the lower energy.

In Fig. 10 we show the individual contributions to the differential transmission at a probe of 2.0 eV. The holes make a major contribution to the total differential transmission. On the long-time scale the electrons contribute more to the differential transmission because they have a lower density of states than the holes. The electron contribution due to the split-off transition eventually dominates as electrons return from the satellite valleys and relax by polar-optical phonons to the bottom of the band.

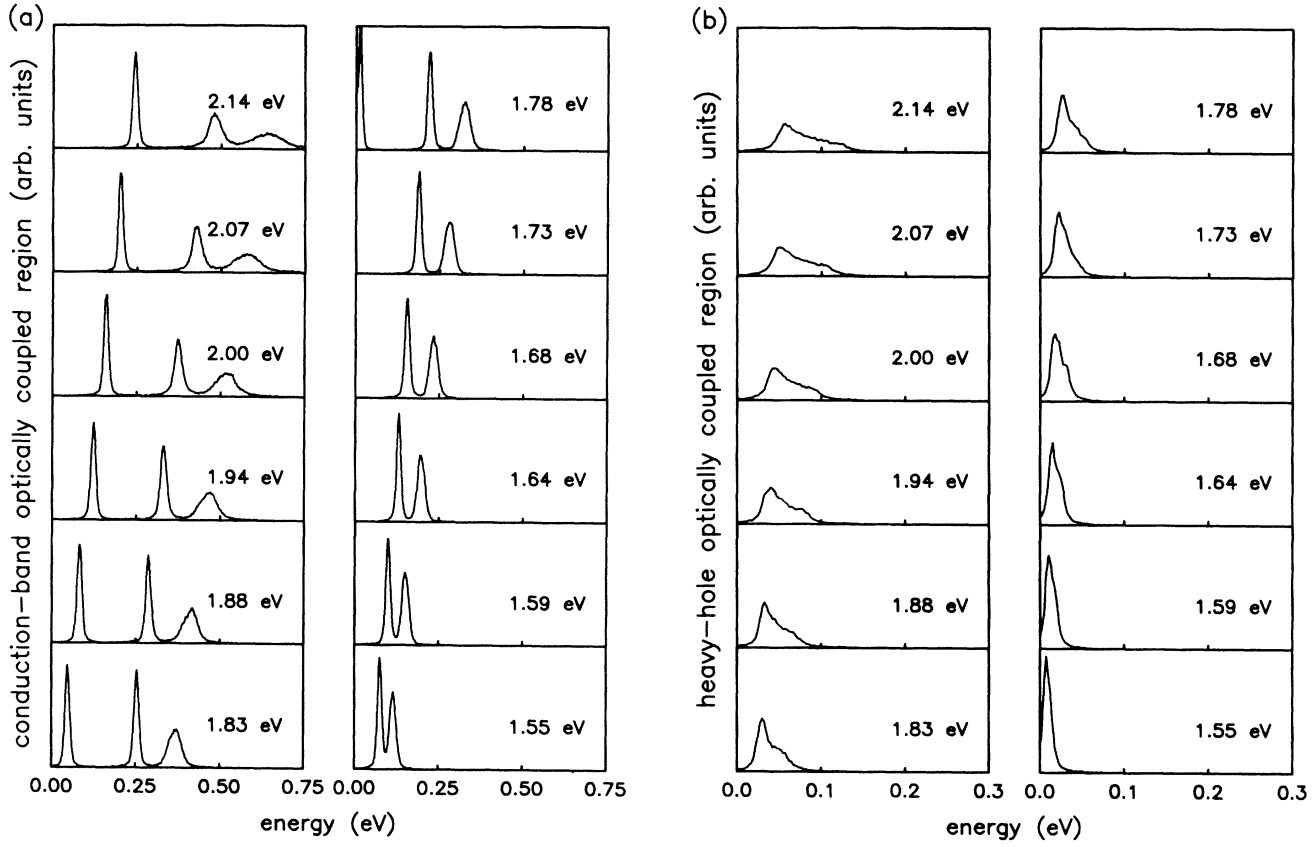

FIG. 8. (a) Conduction-band optically coupled region in GaAs for 75-fs photoexcitation. The split-off transition is not allowed for laser energies of 1.73 eV and lower. Broadening is caused by the laser linewidth, by collisional broadening, and by band-structure anisotropy. (b) Heavy-hole band optically coupled region in GaAs for 75-fs photoexcitation. Band-structure anisotropy causes the optically coupled region to widen with increasing energy.

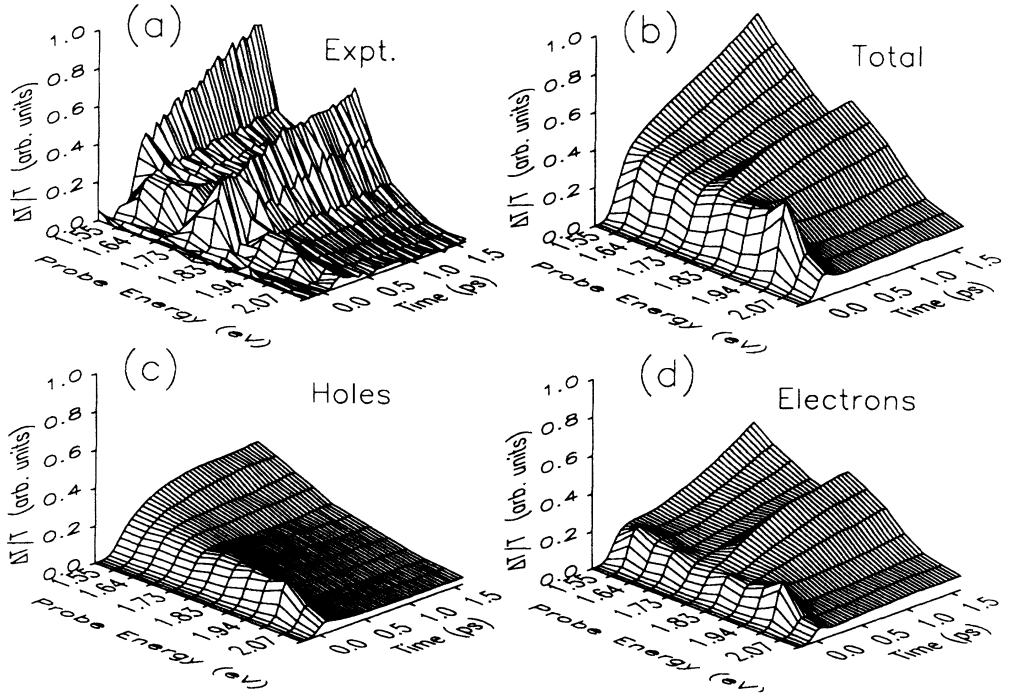

FIG. 9. (a) Experimental differential transmission spectra from Schoenlein *et al.* (Ref. 1) compared with (b) calculated differential transmission spectra including both electrons and holes, (c) including only holes, and (d) including only electrons. Neither (c) nor (d) alone match the experimental measurements as well as (b). Experimental data are provided courtesy of J. Fujimoto.

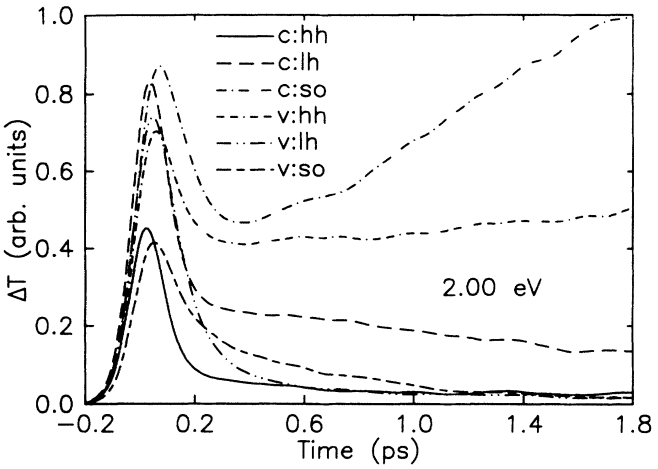

FIG. 10. Relative contributions to differential transmission in electron and hole bands for each transition for a 2.0-eV pump and probe. In the key, c or v indicates whether the contribution is from carriers in the conduction or valence (hole) band, and hh, lh, or so denotes whether the optical transition is from the heavy, light, or split-off hole band. Holes contribute on the same scale as electrons. After the initial transient, the portion of the differential transmission attributable to the split-off transition in the conduction band rises as electrons reenter the Γ valley from the satellite valley.

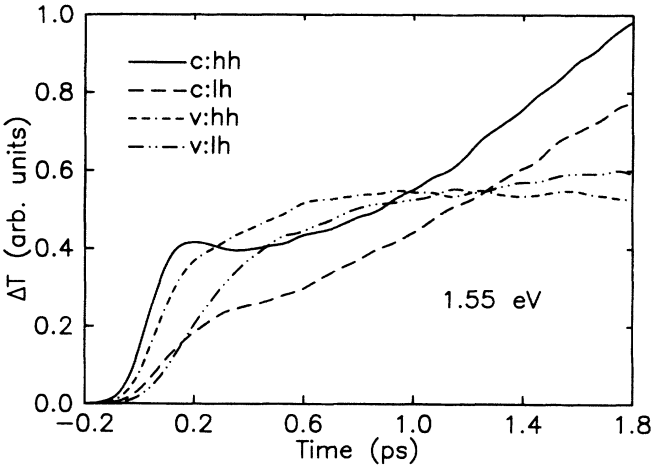

FIG. 11. Relative contributions to the differential transmission in electron and hole bands for each transition for 2.0-eV pump and 1.55-eV probe. In the key, c or v indicates whether the contribution is for the conduction or valence (hole) band, and hh or lh denotes the optical transition as from the heavy or light hole. Because they are excited at the top of the band, heavy holes are responsible for a significant fraction of the initial rise in the differential transmission. Electrons also make a large contribution to the initial transient, primarily because the 1.55-eV pulse probes immediately below the 2.0-eV transition from the split-off-hole band. On the long-time scale the electrons contribute the most to the differential transmission because they have a lower density of states than the holes.

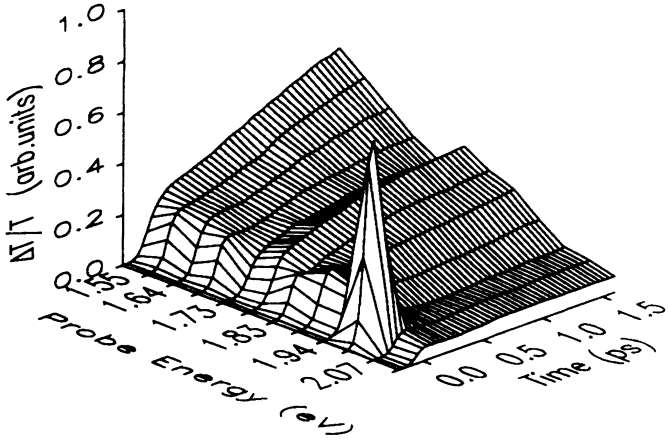

FIG. 12. Total calculated differential transmission spectra without the effects of collisional broadening. Figure 9(b) provides a much better match to Fig. 9(a) than this figure. Without collisional broadening the initial transient at the pump energy is much too large.

In Fig. 11 we show the individual contributions to the differential transmission at 1.55 eV. Part of the initial rise in the solid line for the electrons occurs because the 1.55-eV heavy-hole transition probes the 2.0-eV split-off transition in the conduction band (cf. Fig. 8). The initial rise in the differential transmission at low energy is also due to the rapid redistribution of holes.

The calculated results of pump–continuum-probe spectra without the inclusion of collisional broadening are shown in Fig. 12. Figure 9(b) provides a much better match to the experimental results, Fig. 9(a), than Fig. 12 because the differential transmission without collsional broadening at the pump energy, 2.0 eV, is much too large. Collisional broadening has the effect of lowering the initial transient by decreasing the overlap between pump and probe pulses. Including collisional broadening in the calculation of the initial excitation and the differential transmission are, therefore, essential components of the theory.

B. 2-eV pump-probe simulations

In Fig. 13 the normalized differential transmissions for excitation densities of 10^{17} and 10^{18} cm^{-3} are shown for both experiments and simulations. There is a good general fit with the data, especially on the short-time scale for all data. The concentration dependence of the experiments after the initial transient is not reproduced by the simulations. This is not critical to our conclusions because we restrict our analysis to the initial transient. Also, the concentration dependence of the intermediate response is not found in similar experiments by Rosker *et al.*[7] and is still under contention in the literature.

To better understand the physics and judge the reliability of our conclusions, we test the sensitivity of the transmission to several carrier-interaction strengths. Figure 14 shows the results of a series of such simulations for which the optical deformation potential constant for $\Gamma \rightarrow L$ scattering is varied from 2×10^8 to 8×10^8 eV/cm

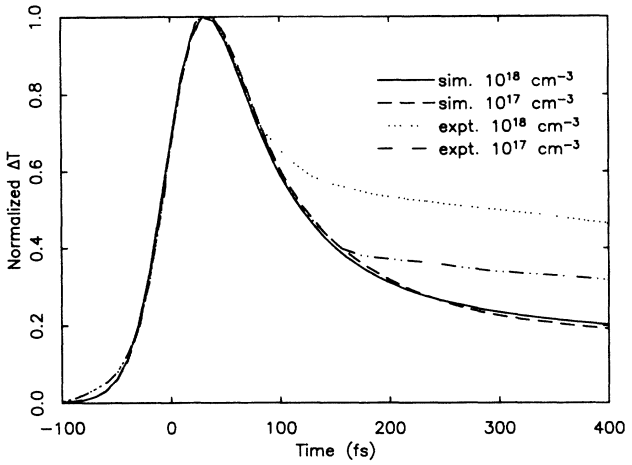

FIG. 13. Comparison of experimental and simulated normalized differential transmission for excitation densities of 10^{18} and 10^{17} cm^{-3}. The calculated initial transient, from which we base our quantitative results, accurately models the experimental results.

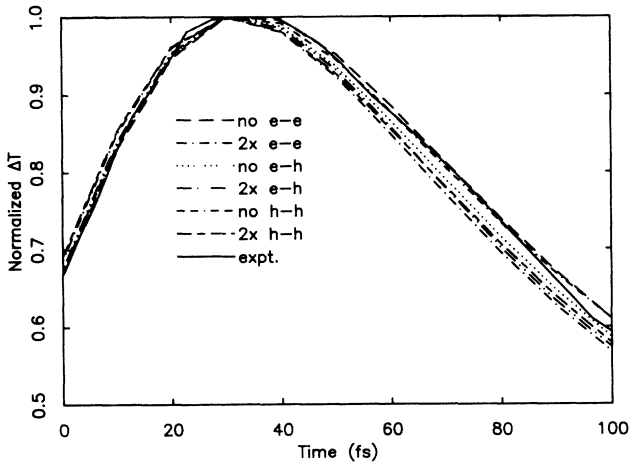

FIG. 15. Normalized differential transmission for part of initial transient for various strengths of carrier-carrier interactions. Initial transient is much less sensitive to changes in the strength of carrier-carrier interactions than it is to variations in $D_{\Gamma\to L}$ (cf. Fig. 14).

and compared with the results from Lin *et al.*[2] Figure 14 shows that the initial transient is highly sensitive to the value of the deformation potential constant and that the best fit occurs for $D_{\Gamma\to L}=5\times10^8$ eV/cm. This is consistent with values in the literature which range from 1.5×10^8 (Ref. 38) to 10^9 eV/cm.[39] Most of the reported results for $D_{\Gamma\to L}$ are between 3×10^8 and 7×10^8 eV/cm.[40–44]

Figure 15 shows the sensitivity of the differential transmission to the rate of carrier-carrier scattering. Initial transients are plotted for runs in which the different carrier-carrier interactions are either doubled or zeroed. The effect is much less dramatic than for intervalley scattering. As shown by Fig. 15, the transmission does not vary significantly at short times, but has some weak dependence at times greater than 300 fs. Considering that carrier-carrier interactions are elastic for the pair, and do not change the energy distribution as directly as intervalley scattering, the small effect that carrier-carrier scattering has on the differential transmission is reasonable.

Therefore, although carrier-carrier scattering may occur at a high rate, this type of experiment does not measure it efficiently (unless, e.g., a continuously tunable probe pulse is used[4,5] or phase coherence is measured[45]). The differential transmission is an integral over the energy width of the probe pulse [cf. Eq. (6)]. Since carrier-carrier interactions in semiconductors do not usually result in a large exchange of energy, a carrier may undergo many carrier-carrier scattering events before it is outside the region sampled by the probe pulse. $\Gamma\to L$ scattering, in contrast, always removes an electron from the probe region. The differential transmission is a measure of the rate at which carriers are removed from the optically connected region, which is not equivalent to the scattering rate.

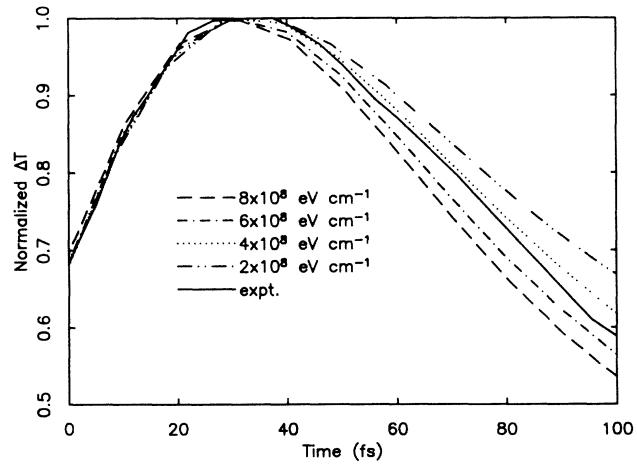

FIG. 14. Normalized differential transmission for part of initial transient for $D_{\Gamma\to L}=0.2$, 0.4, 0.6, and 0.8 eV/cm. Curves show that the width of the initial transient is sensitive to the value of the optical deformation potential constant and that the best fit occurs for $D_{\Gamma\to L}=5\times10^8$ eV/cm.

IV. CONCLUSIONS

We obtain quantitative results from femtosecond laser spectroscopy measurements in GaAs by calculating the nonlinear absorption and using an ensemble Monte Carlo method to model both electrons and holes. Density of states, Bloch overlap factors, and optical matrix elements are determined by a 30-band $\mathbf{k}\cdot\mathbf{p}$ method to realistically include hole band-structure effects. Unlike previous calculations, our method models carrier dynamics according to the Boltzmann transport equation and provides a direct link to the experimental results.

The simulations match continuum-probe data over a large range of energies, and thus establishes the reliability of the model. We find that holes must be included in all aspects of the model, and that it is essential to include collisional broadening in the calculation of the nonlinear absorption.

The band-structure calculations show that using the

effective-mass approximation for holes will lead to considerable error. Anisotropy and nonparabolicity become critical factors away from the band edge.

The intervalley deformation potential constant for $\Gamma \rightarrow L$ scattering is found to be 5×10^8 eV/cm by comparing the sensitivity of Monte Carlo parameters with experimental data. Tests of the sensitivity to the differential transmission are also used to show that these experiments are not an effective measure of carrier-carrier scattering rates.

ACKNOWLEDGMENTS

We are grateful to J. Fujimoto for his suggestions and generous cooperation. Y. C. Chang provided us with the $\mathbf{k}\cdot\mathbf{p}$ program. We are also thankful for useful discussions during the development of this work with C. Hooper, B. Mason, L. Sham, and N. Sullivan. This work was supported by the U.S. Defense Advanced Research Projects Agency through Contract No. MDA972-88-J-1006 (D.W.B. and C.J.S.), the U.S. National Science Foundation through Grant No. DMR89-57382 (C.J.S.) and by the U.S. Office of Naval Research through Grant No. N00014-89-J-1470 (D.W.B. and K.H.). Supercomputing time was provided by the National Center fo Supercomputing Applications and the National Center for Computational Electronics at the University of Illinois, and by Cray Research, Inc.

APPENDIX: BLOCH OVERLAP FACTORS

The methods used to calculate and implement Bloch overlap factors in the Monte Carlo simulations of femtosecond laser spectroscopy experiments are described here. As a rule, Bloch overlap factors are important for anisotropic bands.[31] Since the conduction band in GaAs has s-like symmetry and is isotropic close to Γ_1, overlap factors are usually neglected for calculating electron-scattering rates. The heavy-, light-, and split-off-hole bands, however, exhibit p-like symmetry and thus overlap factors should be considered.

According to Bloch's theorem, wave functions of the atomic Hamiltonian for a crystalline solid can be written

$$\Psi_{n\mathbf{k}}(\mathbf{r})=u_{n\mathbf{k}}(\mathbf{r})e^{i\mathbf{k}\cdot\mathbf{r}} , \tag{A1a}$$

$$u_{n\mathbf{k}}(\mathbf{r}+\mathbf{R})=u_{n\mathbf{k}}(\mathbf{r}) , \tag{A1b}$$

where n is the eigenstate number, and $\mathbf{R}$ is the lattice vector. From first-order time perturbation theory, Fermi's golden rule for a transition from $\mathbf{k}$ in band n to $\mathbf{k}'$ in band m is

$$\begin{aligned} S_{nm}(\mathbf{k},\mathbf{k}') &= \frac{2\pi}{\hbar}|H_{m\mathbf{k}'n\mathbf{k}}|^2\,\delta(E_m(\mathbf{k}')-E_n(\mathbf{k})) \\ &= \frac{2\pi}{\hbar}|\beta(\mathbf{k}-\mathbf{k}')|^2\,G_{nm}(\mathbf{k},\mathbf{k}') \\ &\quad\times\delta(E_m(\mathbf{k}')-E_n(\mathbf{k})) , \end{aligned} \tag{A2}$$

where the Bloch overlap factor is

$$G_{nm}(\mathbf{k},\mathbf{k}')=\tfrac{1}{2}\sum_{s,s'}\left|\int u^*_{n\mathbf{k}}(\mathbf{r})u_{m\mathbf{k}'}(\mathbf{r})d\mathbf{r}\right|^2 . \tag{A3}$$

In this Appendix all integrals are over the primitive cell. Using the $\mathbf{k}=\mathbf{0}$ terms of the periodic part of the Bloch states as a finite basis set, $\mathbf{k}\neq\mathbf{0}$ terms can be expanded as

$$u_{n\mathbf{k}}(\mathbf{r})=\sum_i c^k_{ni}u_{i0}(\mathbf{r}) . \tag{A4}$$

Then

$$\begin{aligned} G_{nm}(\mathbf{k},\mathbf{k}') &= \tfrac{1}{2}\sum_{s,s'}\left|\sum_{i,j}(c^{\mathbf{k}}_{ni})^*c^{\mathbf{k}'}_{mj}\int u^*_{i0}(\mathbf{r})u_{j0}(\mathbf{r})dr\right|^2 \\ &= \tfrac{1}{2}\sum_{s,s'}\left|\sum_i(c^{\mathbf{k}}_{ni})^*c^{\mathbf{k}'}_{mi}\right|^2 , \end{aligned} \tag{A5}$$

where the orthonormality of Ψ,

$$\int\Psi^*_{i\mathbf{k}}(\mathbf{r})\Psi_{j\mathbf{k}}(\mathbf{r})d\mathbf{r}=\delta_{i,j} , \tag{A6}$$

has been invoked for $\mathbf{k}=\mathbf{0}$.

Ideally, $G_{nm}(\mathbf{k},\mathbf{k}')$ is calculated directly from the $\mathbf{k}\cdot\mathbf{p}$ method each time a hole-scattering event occurs in the Monte Carlo simulation. This method, however, consumes an excessive amount of computer time. On the other hand, completely storing $G_{nm}(\mathbf{k},\mathbf{k}')$ for all magnitudes and angles of $\mathbf{k}$ and $\mathbf{k}'$ requires a prohibitively large allocation of memory. The compromise used in these simulations is to approximate $G_{nm}(\mathbf{k},\mathbf{k}')$ by $G_{nm}(k,k',\theta)$, where θ is the angle between $\mathbf{k}$ and $\mathbf{k}'$.

Within this approximation, however, directions of the initial and final vectors are neglected. Therefore, for each element of $G_{nm}(k,k',\theta)$ 50 (an arbitrary number) initial k vectors of a given magnitude randomly distributed over $2\pi\Omega$ are chosen. The corresponding final vectors are selected for a given θ and magnitude, but randomly distributed over ϕ (2π) in the initial vector reference frame (i.e., $\mathbf{k}$ is along $\theta=0$). The final vector is then projected onto the original reference frame. Overlap factors are calculated for each pair, and the average of 50 pairs stored for use in the Monte Carlo simulations.

[1]R. W. Schoenlein, W. Z. Lin, S. D. Brorson, E. P. Ippen, and J. G. Fujimoto, Appl. Phys. Lett. **51**, 1442 (1987).

[2]W. Z. Lin, J. G. Fujimoto, E. P. Ippen, and R. A. Logan, Appl. Phys. Lett. **51**, 161 (1987).

[3]W. Z. Lin, R. W. Schoenlein, J. G. Fujimoto, and E. P. Ippen, IEEE J. Quantum Electron. **QE-24**, 267 (1988).

[4]W. H. Knox, C. Hirlimann, D. A. B. Miller, J. Shah, D. S. Chemla, and C. V. Shank, Phys. Rev. Lett. **56**, 1191 (1986).

[5]J. L. Oudar, D. Hulin, A. Migus, A. Antonetti, and F. Alexandre, Phys. Rev. Lett. **55**, 2074 (1985).

[6]C. W. W. Bradley, R. A. Taylor, and J. F. Ryan, Solid-State Electron. **32**, 1173 (1989).

[7]M. Rosker, F. Wise, and C. L. Tang, Appl. Phys. Lett. **49**, 1726 (1986).

[8]W. Z. Lin, J. G. Fujimoto, E. P. Ippen, and R. A. Logan, Appl. Phys. Lett. **50**, 124 (1987).

[9]P. C. Becker, H. L. Fragnito, C. H. Brito Cruz, J. Shah, R. L. Fork, J. E. Cunningham, J. E. Henry, and C. V. Shank, Appl. Phys. Lett. **53**, 2089 (1988).
[10]B. S. Wherrett, A. L. Smirl, and T. F. Boggess, IEEE J. Quantum Electron. **QE-19**, 680 (1983).
[11]D. J. Erskine, Ph.D. dissertation, Cornell University Press, Ithaca, NY, 1984.
[12]D. K. Ferry (private communication).
[13]J. Collet, T. Amand, and M. Pugnet, Phys. Lett. **96A**, 368 (1983).
[14]J. Collet and T. Amand, J. Phys. Chem. Solids **47**, 153 (1986).
[15]M. Asche and O. G. Sarbei, Phys. Status Solidi B **126**, 607 (1984).
[16]M. Asche and O. G. Sarbei, Phys. Status Solidi B **141**, 487 (1987).
[17]C. J. Stanton, D. W. Bailey, K. Hess, and Y. C. Chang, Phys. Rev. B **37**, 6575 (1988).
[18]M. J. Kann, A. M. Kriman, and D. K. Ferry, Solid-State Electron. **32**, 1831 (1989).
[19]M. A. Osman and D. K. Ferry, Phys. Rev. B **36**, 6018 (1987).
[20]Y. C. Chang (private communication).
[21]F. H. Pollak, C. W. Higginbotham, and M. Cardona, J. Phys. Soc. Jpn. Suppl. **21**, 20 (1966).
[22]S. Adachi, J. Appl. Phys. **58**, R1 (1985).
[23]J. S. Blakemore, J. Appl. Phys. **53**, R123 (1982).
[24]D. E. Aspnes, S. M. Kelso, R. A. Logan, and R. Bhat, J. Appl. Phys. **60**, 754 (1986).
[25]Discontinuities at the K and U points arise because of the finite size of the $\mathbf{k}\cdot\mathbf{p}$ basis set which does not explicitly exhibit cubic symmetry. Since transitions only occur near the Γ point for 2-eV photoexcitation, inaccuracies in the band structure near the zone boundary are not crucial to our calculations.
[26]G. Gilat and L. J. Raubenheimer, Phys. Rev. **144**, 390 (1966).
[27]G. Gilat and Z. Kam, Phys. Rev. Lett. **22**, 715 (1969).
[28]K. Brennan and K. Hess, Phys. Rev. B **29**, 5581 (1984).
[29]K. Sadra, C. M. Maziar, B. G. Streetman, and D. S. Tang, J. Appl. Phys. **66**, 4791 (1989).
[30]Even for $k=0$, Wiley's expression is not exact since it neglects coupling to higher bands.
[31]J. D. Wiley, in *Semiconductors and Semimetals,* edited by R. K. Willardson and A. C. Beers (Academic, New York, 1971), Vol. 6.
[32]C. Jacoboni and L. Reggiani, Rev. Mod. Phys. **55**, 645 (1983).
[33]Y. C. Chang, D. Z.-Y. Ting, J. Y. Tang, and K. Hess, Appl. Phys. Lett. **42**, 76 (1983).
[34]K. Kim, B. A. Mason, and K. Hess, Phys. Rev. B **36**, 6547 (1987).
[35]P. J. Price, in *Semiconductors and Semimetals,* edited by R. K. Willardson and A. C. Beers (Academic, New York, 1979), Vol. 14.
[36]M. Costato and L. Regianni, Phys. Status Solidi B **59**, 47 (1973).
[37]M. Costato and L. Regianni, Phys. Status Solidi B **59**, 471 (1973).
[38]C. L. Collins and P. Y. Yu, Phys. Rev. B **30**, 4501 (1984).
[39]M. A. Littlejohn, J. R. Hauser, and T. H. Glisson, J. Appl. Phys. **48**, 4587 (1977).
[40]S. Zollner, S. Gopalan, and M. Cardona, Appl. Phys. Lett. **54**, 614 (1989).
[41]D. N. Mirlin, I. Ya. Karlik, and V. F. Sapega, Solid State Commun. **65**, 171 (1988).
[42]M. Heiblum, E. Calleja, I. M. Anderson, W. P. Dumke, and C. M. Osterling, Phys. Rev. Lett. **56**, 2854 (1986).
[43]S. Krishnamurthy, A. Sher, and A.-B. Chen, Appl. Phys. Lett. **53**, 1853 (1988).
[44]J. Shah, B. Deveaud, T. C. Damen, W. T. Tsang, A. C. Gossard, and P. Lugli, Phys. Rev. Lett. **59**, 2222 (1987).
[45]P. C. Becker, H. L. Fragnito, C. H. Brito Cruz, R. L. Fork, J. E. Cunningham, J. E. Henry, and C. V. Shank, Phys. Rev. Lett. **61**, 1647 (1988).
[46]B. R. Nag, *Electron Transport in Compound Semiconductors* (Springer-Verlag, New York, 1980).